BONE

Volumetric spatial decomposition of trabecular bone into rods and plates—A new method for local bone morphometry

Martin Stauber, Ralph Müller *

Institute for Biomedical Engineering, Swiss Federal Institute of Technology (ETH) and University of Zürich, Moussonstrasse 18, CH-8044 Zürich, Switzerland

Abstract

Bone microarchitecture is believed to play a key role in determining bone quality. We therefore present a new method for the volumetric spatial decomposition of trabecular bone samples into its basic elements (rods and plates). This new method is a framework for the element based description of bone microarchitecture. First, the newly developed algorithm was validated on computer-generated models. Then, it was applied to 328 human trabecular bone samples harvested from 70 donors at five different anatomical sites (calcaneus, femoral head, iliac crest, lumbar spine 2 and 4), which were previously scanned by microcomputed tomography. Standard three-dimensional morphometric algorithms were used to analyze the trabeculae on an individual basis with respect to their volume, surface, and thickness. The results were statistically compared for the five sites. In this study, it was possible for the first time to spatially decompose trabecular bone structures in its volumetric elements; rods and plates. The size of the largest element in the structures showed significant differences for the five compared sites. In samples from femoral head, we found that basically one "major element" was spanning through the whole structure whereas in lumbar spine and calcaneus, smaller elements dominate. From this, we suggest that the strength of strong, dense plate-like structures is determined by the major elements whereas in looser rod-like structures the strength is given by the arrangement, quality, and shape of a whole set of elements. Furthermore, we found that globally determined structural indices such as the mean curvature of the bone surface (<H>) or related to this the structure model index (SMI) are almost exclusively explained by the arrangement of the plates. This also suggests that rods hold independent information characterizing trabecular bone quality, especially in the spine. These findings may improve the understanding of the site-specific role of bone microarchitecture in determining bone quality and in future studies the competence of bone.
© 2005 Elsevier Inc. All rights reserved.

Keywords: Trabecular bone architecture; Bone strength; Bone quality; Local morphometry; Volumetric spatial decomposition

Introduction

Osteoporosis is defined as a skeletal disorder characterized by compromised bone strength predisposing to an increased risk of fracture. Bone strength reflects the integration of two main features: bone mineral density expressed as grams of mineral per area or volume and bone quality referring to bone architecture, turnover, damage accumulation, and mineralization [3]. Thus, it is not unexpected that older persons may lose bone, as expressed by a decrease in bone density, but do not develop fractures. Bone mineral density, geometry of bone, microarchitecture of bone, and quality of the bone material are all components that determine bone strength as defined by the bone's ability to withstand loading [18,35]. For this reason, microstructural information must be included in the analysis to predict individual mechanical bone properties [31,37].

Bone microarchitecture can easily be assessed in vitro by means of microcomputed tomography (μCT) [45] and in peripheral regions in vivo by quantitative-computed tomography (QCT) [32,33] and magnetic resonance imaging (MRI) [24,25,51]. In this paper, we will concentrate on images acquired with μCT, a non-destructive technique with high spatial resolution. The basic morphometric measures are the relative bone volume density (BV/TV) and bone surface to bone volume ratio (BS/BV). Additional to these basic parameters, the

* Corresponding author. Fax: +41 44 632 1214.
  E-mail addresses: stauber@biomed.ee.ethz.ch (M. Stauber),
ralph.mueller@ethz.ch (R. Müller).

mean trabecular thickness (Tb.Th), the mean trabecular separation (Tb.Sp), and the trabecular number (Tb.N) are often determined parameters that can be computed directly from the three-dimensional image without an underlying model assumption [11]. To estimate the plate–rod characteristic of a trabecular bone structure, a parameter called structure model index (SMI) was invented [12], which is 0 and 3 for an ideal plate structure and an ideal rod structure, respectively. It was shown that the SMI is closely related to mean curvature <H> of the bone surface [17]. Also related is the trabecular bone pattern factor (TBPf) [9]. It can be shown that this parameter equals 2 <H> if extended to the third dimension. Mean intercept length (MIL) and other measures of the extent of architectural anisotropy such as volume orientation, star volume distribution, or star length distribution [36] were used to improve the prediction of multiaxial elastic properties of trabecular bone from bone volume density alone [53]. Using finite element models, the apparent stiffness, which is an important inherent attribute of trabecular bone samples, can be computed directly and very accurately [13,50].

The methods mentioned so far all are an attempt to relate the properties of trabecular bone microstructure on a global basis to bone quality. Only few attempts have been made to investigate truly local parameters of the trabecular network. Pothuaud et al. [42] presented a method called line skeleton graph analysis (LSGA) to compute topological parameters as well as the length and volume of single trabecular elements. They showed that LSGA can be applied in vivo [41] and has the potential to improve the prediction of mechanical properties when combined with bone volume fraction [43]. Their method, however, was based on a line-skeleton where shape information was lost and an identification of plates and rods was not possible. An attempt to also assess shape information was done by Saha et al. [49], who first introduced a method for the digital topological characterization of the trabecular bone architecture. Their method is based on a thinning algorithm [48] followed by a classification algorithm [46] and allowed them to subdivide the trabecular structure into its rods and plates. This method was later used for orientation analyses of the trabecular bone networks [7] and it could be shown that the locally determined orientations better described anisotropy than MIL.

In this study, we present a new approach, conceptually combining the three-dimensional identification of trabecular elements [42] with the classification of shape preserved skeletons [46]. In contrary to earlier studies, we do not analyze the skeleton but present a method to decompose the trabecular structure into its basic elements (i.e. rods and plates) in its full three-dimensional and volumetric extent. This enables to compute morphological parameters for each element within the trabecular bone structure allowing for the first time to investigate truly local morphometric parameters of the trabecular bone network for rods and plates separately. The specific goals of this study were to 1) present the new volumetric spatial decomposition algorithm, 2) to validate this algorithm, and 3) to use the method for the morphometric description of site-specific differences.

Methods

This section is structured in three parts. In the first part, we describe the newly introduced algorithm to spatially decompose porous structures such as trabecular bone into its underlying elements. The second part shows three mathematical models that were used for the verification of the algorithm. Finally, in the third part, we applied the new algorithm to a set of 328 human trabecular bone structures from five different anatomical sites, which are calcaneus, femoral head, iliac crest, second lumbar spine, and fourth lumbar spine. These samples have previously been described as part of the European Union BIOMED I Concerted Action "Assessment of Bone Quality in Osteoporosis" [5,10].

The spatial decomposition of trabecular bone

In this section, we present a new method for the spatial decomposition of trabecular bone into plate and rod elements. For this, we need a binary three-dimensional image, where bone is separated from other tissues and background, as a starting point. A detailed description on digital topology in three dimensions can be found elsewhere [19,20,29,44].

In this paper, we present a skeletonization approach, where we use the term *skeletonization* for an algorithm that transforms a 3D binary image into a new 3D binary image, denoted as *skeleton*, that has the same topology and shape information but which is only one voxel thick. Although this definition seems to determine the skeleton of an object pretty well, there are infinite ways one can think of on how to compute such a skeleton and many different approaches have already been proposed [1,8,21–23,26–28,30,47,48,52]. In this paper, we used a series of algorithms to compute the final skeleton. In a first step, we computed a very rough two-voxel-thick skeleton using the MB-3D algorithm proposed by Manzanera et al. in 2D [27], 3D [1,26], and *n*D [28]. This algorithm is computationally fast, shape-preserving, and homotopic.

In order to reduce the MB-3D skeleton to a one-voxel-thick skeleton, we introduce a new algorithm, subsequently called *conditional erosion* (CE-3D). It is a fully parallel algorithm that can be applied to any two-voxel-thick skeleton. To remove all dispensable points, the algorithm runs in 6 subsequent scans whereby the structuring element γ_1 is rotated in all 6 possible directions. In a first step, all points that contain the structuring element γ_1 are marked and stored in a separate image C. In a second step, all points that are needed to maintain topology are stored in image D. Those points are detected by scanning the $3 \times 3 \times 3$ neighborhood of each point for the structuring elements δ_i ($i = 1, 2$), where a point is marked, if δ_i is contained in its $3 \times 3 \times 3$ neighborhood. The third step removes then all points that belong to C but not to D. This algorithm is performed only once. The three structuring elements needed for this algorithm are shown in Fig. 1.

Analyzing these two first procedures results in a one-voxel-thick skeleton of the original image. However, this skeleton is very rough and needs optimization. In a first step, we used a point-classification algorithm that is able to compute for each voxel whether it is a surface point, a surface end point, an arc point, an arc end point, an arc–arc intersection point, an arc–surface intersection point, a surface–surface intersection point, or an isolated point. The basic principle of this algorithm was introduced by Saha and Chaudhuri and is described in details elsewhere [46]. However, we had to modify this algorithm slightly since our skeletons were not ideal. Especially, intersection points could not be detected using the original algorithm.
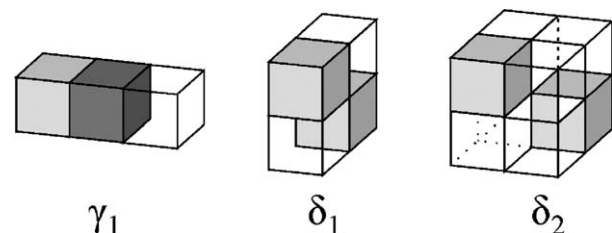

Fig. 1. Structuring elements used by the (A) MB-3D and (B) CE-3D skeletonization algorithm.
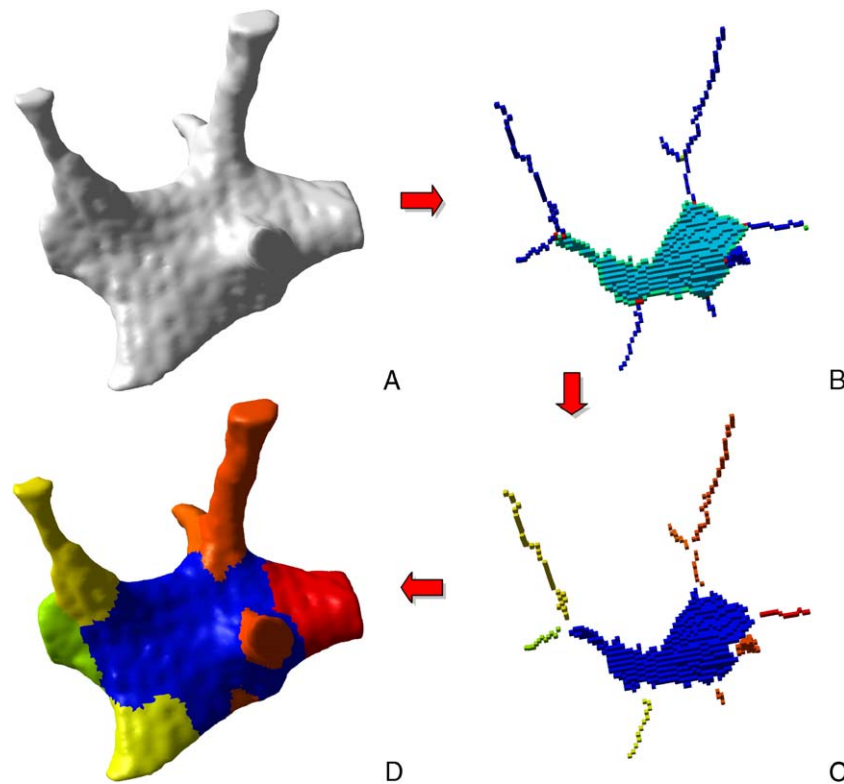
Fig. 2. Spatial decomposition of trabecular bone. The initial binary image that served as input for our algorithm is shown in panel A. A skeletonization and optimization algorithm is applied to get a homotopic shape preserving skeleton as shown in panel B. This skeleton is then point-classified, thus arc-, surface-, border-, and intersection-points are shown in different colors. (C) This point-classified skeleton is then spatially decomposed by removing the intersection points. (D) A two-way multicolor dilation algorithm was applied to find the volumetric extend of each element, yielding in the final spatially decomposed structure.

To the classified skeletons, we then applied two optimization procedures. The first was designed to reduce slender planes, which may appear from rod-like elements with elliptical cross-section, to arcs. To achieve this goal, we removed iteratively all surface-end points, which means that a one-voxel thick boundary was removed from all surfaces. In each iteration, the skeleton was newly classified to retrieve a properly classified skeleton. For the optimization, we used a parameter which we would like to call the *slenderness parameters*. This parameter is simply the number of iterations applied to reduce the surfaces. The second algorithm was invented to remove end-arcs (an end-arc is an arc where one node is an arc end point) arising from surface noise. For this purpose, each rod which was shorter than a critical length was removed from the skeleton. The critical length defines a new parameter which we would like to call *noise parameter n*. A sensitivity study of these two model parameters

showed that the noise parameter n had only a minor effect on the skeleton when set to twice the value of the slenderness parameter s, which leaves the model with one single optimization parameter s. In this study, the model parameter s was set to 10, which proved to yield in visually reasonable results for all computer-generated models (Fig. 3) as well as for all human trabecular bone samples at all sites (Fig. 4). The elements in the computer models were perfectly identified independent of their relative size and thickness. Also, the inspection of the decomposed human bone structures showed good results in all sites using this parameter for optimization. Additionally, this value was supported by the sensitivity analysis, where we found that, although decomposition was sensitive to the parameter setting, the derived morphometric indices were well behaved where an increase of s by one caused an average change in local morphometric indices of about 1.8%. However, this parameter
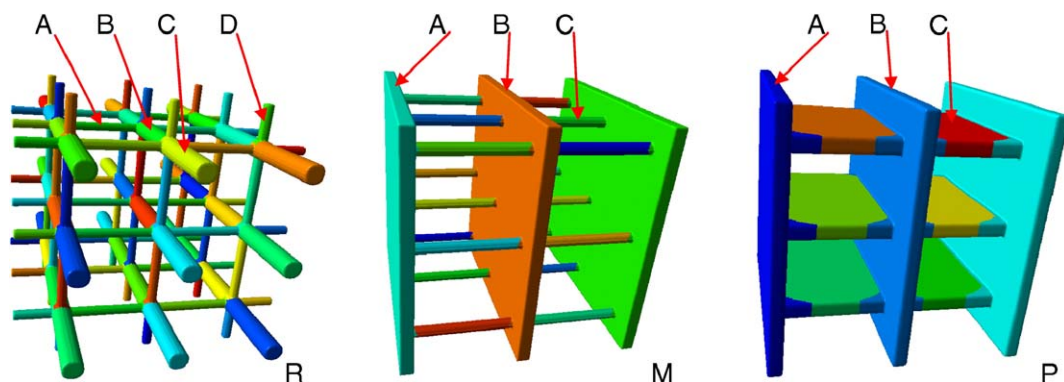

Fig. 3. The three computer-generated models used for the validation of the algorithm. To represent a wide variety of structures, a (R) rod, a (M) mixed, and a (P) plate model were produced. The elements of these three models are: R_A thin inner rod, R_B thick inner rod, R_C thick outer rod, and R_D thin outer rod for the rod model, M_A outer-plate, M_B inner-plate, and M_C interconnecting rods for the mixed model, and P_A outer-plate, P_B inner-plate, P_C interconnecting-plate for the plate model.

may have to be adapted when changing to a different resolution or a different species, similar to the settings for the Gaussian filtration and the global threshold used to binarize the images.

The image processing steps from the original image up to the optimized skeleton are visualized in Fig. 2, where step A shows the original specimen and B shows the corresponding skeletonized and optimized point classified step.

This optimized skeleton served as the basis for spatial decomposition. The principal idea was to decompose the skeleton into its arcs and plates by identifying the elements in-between the intersection points. Arcs were defined as all arc-type voxels bound by two voxels being either an arc–arc intersection point, an arc end point, or an arc–surface intersection point. Plates were defined as the points bound by surface–end points, surface–surface intersection points, and arc–surface intersection points. These arcs and surfaces were later used for the discrimination of rods and plates. After the thinning and optimization procedures, configurations could appear where two nodes were very close to each other. The interconnecting arc was then only a few voxels in length and it was therefore reasonable to remove this artificial arc and to identify these two nodes as one single node. To achieve this, we deleted all voxels around the intersection points within a sphere of radius two. After this operation, single elements in the skeleton could be identified and were written to a new image, where each such element was assigned a number. We used even numbers for the plate-like elements and odd numbers for the rod-like elements. This procedure is visualized in Fig. 2C, where each element has a different color.

In a last step, we had to identify the volumetric extend of the elements in the spatially decomposed image. For this purpose, we used a dilation-related algorithm. The image was scanned alternating in forward and backward direction in order not to favor one direction only. In each scan, a morphological dilation with a 26-neighbor structuring-element was applied and the new voxels were set to the color (or number) of the current voxel, where the new voxel could only be set if it was not already occupied by a neighboring element. The alternating forward–backward scanning also prevented that one element could grow on expense of a neighboring element and resulted in logical element-interfaces. We would like to call this procedure *multicolor dilation*. Additionally, to maintain the overall shape and volume of the structure, voxels were only set if they were also present in the original binary image. This operation yielded in a spatially decomposed image of the original structure where each element was assigned a number. Elements arising from arcs were identified to be rods and elements arising from surfaces were identified to be plates. The visualization of this last step is done in Fig. 2D. The different numbers of the elements are visualized by different colors in the image.

Local morphometry

Such spatially decomposed structures may serve as a basis for many new investigations and subsequent algorithms. In this study, we used them to compute local morphometric indices on a trabecular level, i.e. morphometry as applied to individual rods and plates as identified directly from the three-dimensional images. In order to follow the naming conventions proposed by Parfitt et al. [38], we suggest to use the prefix Pl for plates, Ro for rods, and El for elements that could be either plate or rod. The volume, surface, and thickness of one single element is denoted with V, S, and Th, and the sum of the volume and surface over all elements with BV, and BS, respectively. Furthermore, we use brackets (<>) to denote mean values that are averaged over all elements of the same type.

Basically, all standard three-dimensional morphometric algorithms may be applied to the elements. In this paper, we concentrated on only a few parameters which were the mean volume (<Ro.V>, <Pl.V>), the mean surface (<Ro.S>, <Pl.S>), as well as the mean thickness (<Ro.Th>, <Pl.Th>) averaged for each structure over all rods and plates separately. Furthermore, the plate volume density (Pl.BV/TV), which is defined as total plate volume divided by total volume of interest in percent and the rod volume density (Ro.BV/TV), which is defined as the total rod volume divided by total volume of interest in percent, as well as the relative bone volume fraction of plates (Pl.BV/BV) and rods (Ro.BV/BV = 100% − Pl.BV/BV) in percentage, were determined. Another parameter investigated was the relative size of "major elements" (El.V$_{max}$ / BV), which is defined as the volume of the largest element divided by total bone volume. All parameters were computed using standard morphometric algorithms as

implemented in the image processing language IPL (Version 4.28d; Scanco Medical AG, Switzerland).

Validation of the algorithm on computer-generated images

For the validation of the algorithm, three computer-generated models representing a rod-like (R), a mixed (M), and a plate-like (P) structure were produced. The three models are shown in Fig. 3 and the dimensions of their elements are given in Table 1. The edge-length of a voxel was chosen to be 10 μm in each direction in order to present typical dimensions as found in trabecular architectures.

Each model was spatially decomposed with the newly developed algorithm, and the mean volume (<El.V>), surface (<El.S>), and thickness (<El.Th>) was computed for each element using standard 3D morphometry. For each element type, the mean value and standard deviation of those indices was then computed. The same indices were also computed analytically and the results were compared to the morphometric data (Table 2). For the analytic solution, dimensions of the elements ranged from a maximal to a minimal size. This was due to the fact that different mathematically defined objects may represent the same digital object. A digital cylinder of 11 voxels (110 μm) in diameter, for instance, may be represented by all mathematically defined cylinders with diameters in the range of 9 to 11 voxels (90 to 110 μm).

Anatomical data of human trabecular bone

In order to test the newly developed algorithm on real structures, we applied our method to the large data set of human trabecular bone samples from the European Union BIOMED I Concerted Action "Assessment of Bone Quality in Osteoporosis" [5,10]. The analyzed data set encompasses 328 samples harvested from 70 donors (32 females, 38 males with ages ranging from 23 to 92 years; mean 69.4, SD 15.4 years). The samples were harvested from five different anatomical sites; femoral head (FH, $n = 64$), iliac crest (IC, $n = 59$), calcaneus (CA, $n = 69$), second lumbar spine (L2, $n = 67$), and fourth lumbar spine (L4, $n = 69$). All samples were scanned using a microcomputed tomography (μCT) system (μCT 20, Scanco Medical AG, Switzerland) providing a spatial resolution of 28 μm. This system and scanning procedure is described elsewhere in detail [45]. The data set has previously been used for several investigations [10,34]. A 4 mm cubic region of interest (TV) was selected from all samples. Using Gaussian filtration and global thresholding [10], binary images were created presenting either bone or background. A component labeling algorithm was applied to the binary images to remove all parts not 6-connected to the main structure. These images served then as the basis for the proposed spatial decomposition algorithm, which was applied using an optimization parameter of 10. For visual inspection of the outcome of the proposed algorithm, spatially decomposed structures of the five anatomical sites of an arbitrary donor (37-year-old man) were visualized (Fig. 4).

The spatially decomposed structures have been analyzed using the GNU statistical computation and graphics package R (Version 1.7.1; http://www.r-project.org). For each structure, we averaged the morphometric indices; for all rods and for all plates (Table 3, Fig. 5). For each morphometric index, the mean values of all structures were compiled in a box-plot where the five site-groups were compared. Box-plots show the median value enclosed by a box holding 50% of the data spanned by the first and the third quartile. The whiskers show the range of the data, except some outliers that are shown separately by a small circle. The five groups were compared for significant differences ($P < 0.05$) using a pairwise t-test with Bonferroni correction for

Table 1

Dimension of the elements composing the three computer-generated models shown in Fig. 3

Model element	R$_A$	R$_B$	R$_C$	R$_D$	M$_A$	M$_B$	M$_C$	P$_A$	P$_B$	P$_C$
Diameter (voxel)	11	21	21	11	–	–	9	–	–	–
Length (voxel)	100	100	100	50	181	181	71	181	181	121
Width (voxel)	–	–	–	–	181	181	–	181	181	71
Thickness (voxel)	–	–	–	–	9	9	–	9	9	11

In all models, the voxels were chosen to be $10 \times 10 \times 10$ μm^3.

Table 2
Morphometric and analytic results of three computer-generated models used for the validation of the algorithm

Model element		R_A	R_B	R_C	R_D
<El.V> meas.	106 μm³	7.56 ± 0.09	29.4 ± 0.0	30.7 ± 0.02	3.82 ± 0.05
<El.V> anal.		5.57–8.60	26.2–33.1	26.2–33.1	2.39–3.85
<El.S> meas.	103 μm²	2.84 ± 0.02	5.84 ± 0.00	6.69 ± 0.02	1.51 ± 0.01
<El.S> anal.		2.47–3.13	5.52–6.30	6.13–6.94	1.42–1.82
<El.Th> meas.	μm	87.7 ± 0.0	189.6 ± 0.0	189.4 ± 0.0	87.6 ± 0.3
<El.Th> anal.		90–110	190–210	190–210	90–110

Model-element		M_A	M_B	M_C	
<El.V> meas.	106 μm³	294 ± 0	294 ± 0	3.42 ± 0.00	
<El.V> anal.		224–295	224–295	2.73–4.52	
<El.S> meas.	103 μm²	70.9 ± 0.01	69.8 ± 0.00	1.74 ± 0.00	
<El.S> anal.		68.5–71.7	67.9–71.3	1.52–2.01	
<El.Th> meas.	μm	90.0 ± 0.0	90.0 ± 0.0	69.5 ± 0.0	
<El.Th> anal.		70–90	70–90	70–90	

Model-element		P_A	P_B	P_C	
<El.V> meas.	106 μm³	305 ± 0	294 ± 0	90.8 ± 0.1	
<El.V> anal.		259–331	259–331	84.0–105	
<El.S> meas.	103 μm²	69.5 ± 0.00	64.4 ± 0.0	14.7 ± 0.0	
<El.S> anal.		65.1–68.8	61.1–65.6	17.7 ± 18.7	
<El.Th> meas.	μm	90.3 ± 0.1	90.4 ± 0.0	109.5 ± 0.0	
<El.Th> anal.		70–90	70–90	90–110	

The table shows the mean values and standard deviations of the locally determined morphometric results as well as the analytic results determined for the three computer-generated models shown in Fig. 3. The labeling of the elements corresponds to the labeling of the elements in Fig. 3.

multiple testing. If two groups did not differ significantly from each other, they were assigned the same letter (e.g. A, B, ...), which was also plotted in the graph. Thus, groups with the same letter did not differ significantly where groups not having the same letter did.

Standard three-dimensional global morphometry was used to determine bone volume density (BV/TV) and the structure model index (SMI). These parameters have previously been reported and tabulated for the BIOMED I data set [10] and were here used for linear regression analysis with the new local morphometric indices (Fig. 6).

Results

The algorithm was first tested on three computer-generated models. In all three cases, the decomposition worked well and the result looked reasonable (Fig. 3). Visual inspection confirmed that the algorithm basically should work on any structure type. The three parameters (<El.V.>, <El.S>, <El.Th>) computed by direct 3D morphometry were lying in the range of the analytically computed indices except for a few cases where the discrepancies between digital and analytical model were obvious (Table 2).

To investigate a realistic data set, we applied our algorithm to 328 cubic bone samples harvested from 70 donors at five different sites; femoral head (FH), iliac crest (IC), calcaneus (CA), and the second and fourth lumbar spine (L2, L4). The samples from the different sites varied dramatically in their architecture representing a unique data set to test new algorithms. All structures were successfully decomposed by the proposed algorithm. Fig. 4 shows the autopsy samples harvested from a 37-year-old male donor at the five different sites. These images show that most elements are separated in a very intuitive way. The L2 specimen represents a typically

rod-like structure. In this structure, the algorithm found many small rod-like elements building a loose trabecular network. Opposed to this, the FH specimen represents a typically plate-like structure. Here, we found one big element spanning through the whole specimen from top to bottom and from one side to the other (dark blue element). We would like to call these very large elements "major elements". These major elements appear in trabecular bone structures that present themselves as a "Swiss cheese", where only few nodes are present in the skeleton resulting in large elements spanning the whole structure.

To investigate the differences between sites in major elements, we computed for each structure the volume of the largest element in percentage of the total bone volume (El. V_{max} / BV). Site-specific distributions are shown in Fig. 5A and Table 3. Some structures have one "strong" major element whereas others seem to be "weaker" structures composed of a loose network of mainly rod-like elements.

The structure type of the groups is also represented by the relative bone volume fraction of plates (Pl.BV/BV). According to Fig. 5B and Table 3, structures of type CA, L2, and L4 may then be classified as typical rod-like structures, whereas the structures of type FH may be classified as typical plate-like structures. IC structures are typically a mix of plate- and rod-like structures yielding in a classification as an intermediate structure. Plate-like structures do not only have a higher relative plate volume but the plates are also slightly larger (Table 3, Fig. 5C). FH and IC had significantly higher values then CA, L2, and L4 structures. Opposed to this, the size of the rods (Table 3, Fig. 5D) could not be related to the structure type as determined by the relative amount of plate volume.
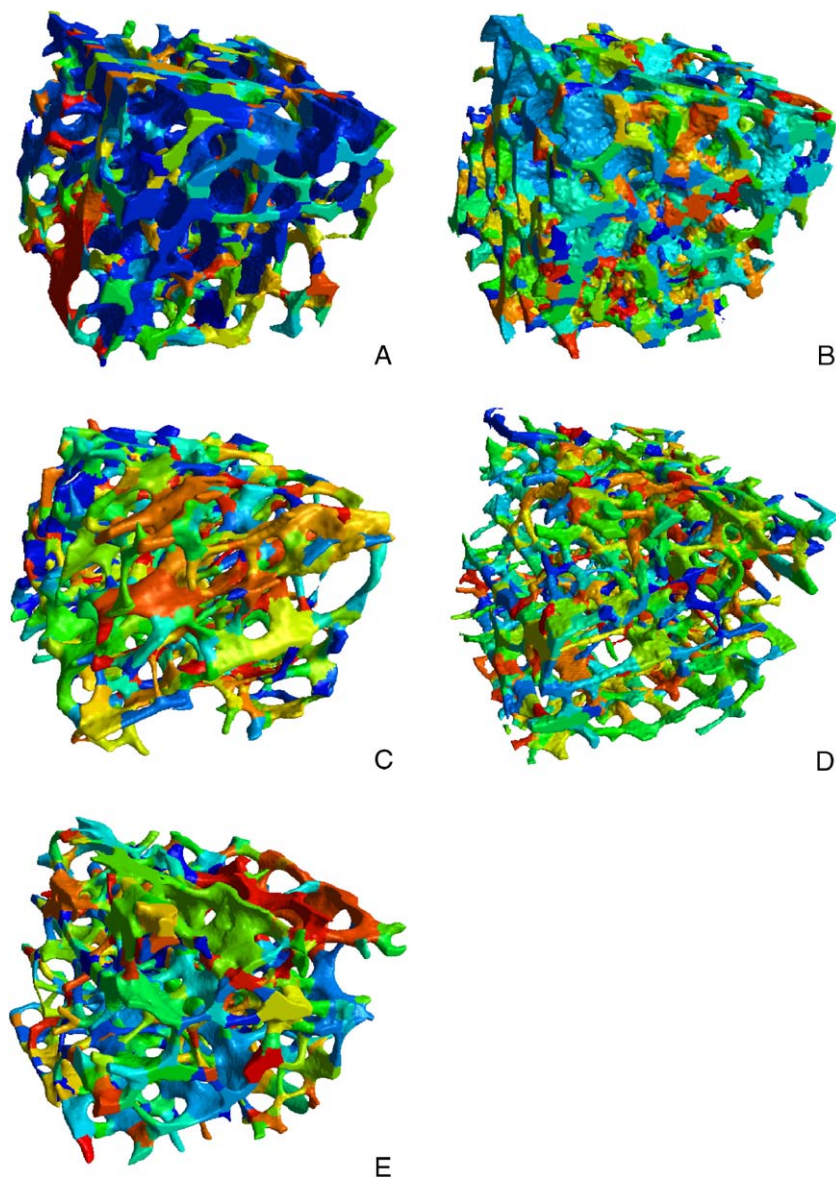
Fig. 4. The spatially decomposed trabecular bone structures of a 37-year-old man from (A) FH—femoral head, (B) IC—iliac crest, (C) CA—calcaneus, (D) L2—second lumbar spine, and (E) L4—fourth lumbar spine.

The values for FH and IC structures were lying in between the values of CA, L2, and L4.

The locally determined bone surface (<El.S>) demonstrates a similar pattern as the locally determined bone volume (<El.V>) for both plates and rods (Table 3). This is not unexpected, since larger elements also have larger surfaces. Opposed to this, element thickness is independent of the trabecular size and does therefore not necessarily reflect <El.V> or <El.S> (Table 3, Figs. 5E and F).

The structure model index (SMI), which in global morphometry is used to determine the rod-likeness or plate-likeness of a trabecular bone sample, was plotted versus the relative bone volume fraction of plates (Pl.BV/BV) (Fig. 6). This relationship could be well described with a logarithmic law ($R^2 = 0.87$) for the whole data set including negative SMI values and with a purely linear law ($R^2 = 0.81$) for the data set where SMI was positive.

Discussion

In this paper, we present a new method that allows for the first time to spatially decompose trabecular bone and into its basic elements; plates and rods. This new method involves several consecutive algorithms that extract the elements from the sample, which then can be analyzed for size, shape, and distributions using standard morphometric algorithms.

Spatial decomposition has been previously described based on line skeletons [41–43] which are not capable to include shape information and hence, cannot distinguish between plates and rods. A line skeleton is an excellent approach for topology analyses but when used for spatial decomposition the results might be difficult to interpret. Thus, these authors put their main interest in the topological analysis of the line skeletons and used the new parameters in combination with global morphometry [43]. Their results showed that local

Table 3
Local morphometric indices of 328 human trabecular bone structures

Index	Site	Mean	SD	CV (%)	Median	Min	Max
<Ro.V>	FH	6.63	1.59	24.0	6.45	3.16	10.34
(10^6 µm³)	IC	6.14	2.05	33.3	5.93	2.04	12.85
	CA	8.15	1.82	22.3	7.71	5.15	14.30
	L2	5.69	1.60	28.1	5.59	2.44	9.90
	L4	7.54	1.94	25.7	7.08	3.33	11.82
<Ro.S>	FH	256	41	16.2	253	159	347
(10^3 µm²)	IC	243	57	23.6	240	113	414
	CA	301	42	14.1	299	231	444
	L2	234	46	19.6	235	129	349
	L4	283	48	17.2	276	164	392
<Ro.Th>	FH	88.3	9.4	10.6	88.4	67.4	105.7
(µm)	IC	79.1	10.2	12.9	78.4	53.1	100.5
	CA	93.3	9.1	9.7	92.6	74.5	119.1
	L2	81.8	9.9	12.1	83.0	58.9	107.2
	L4	92.3	10.7	11.6	92.0	64.5	115.2
<Pl.V>	FH	80.7	43.1	53.3	68.4	12.4	243.4
(10^6 µm³)	IC	69.7	55.3	79.3	61.6	4.6	278.5
	CA	36.8	26.4	71.8	29.8	9.8	145.6
	L2	20.5	13.4	65.7	17.6	5.2	77.7
	L4	32.8	21.8	66.5	29.1	8.0	158.5
<Pl.S>	FH	1550	741	47.9	1416	341	3937
(10^3 µm²)	IC	1689	1242	73.5	1468	175	5918
	CA	970	538	55.5	822	362	3001
	L2	609	316	51.9	527	205	1749
	L4	849	410	48.3	798	284	2559
<Pl.Th>	FH	81.0	6.5	8.0	81.3	71.7	98.7
(µm)	IC	79.4	11.2	14.1	81.0	59.6	108.4
	CA	94.7	9.1	9.6	92.9	75.0	118.1
	L2	83.7	10.4	12.4	83.7	63.7	111.8
	L4	93.1	10.9	11.7	91.3	68.6	118.1
Pl.BV/BV	FH	83.0	10.3	12.4	86.0	51.1	95.7
(%)	IC	65.6	18.4	28.0	69.3	6.0	88.0
	CA	33.8	15.7	46.6	32.4	9.2	71.0
	L2	30.6	13.6	44.6	29.4	7.3	61.4
	L4	34.9	14.2	40.7	35.0	7.6	83.7
El.V$_{max}$ / BV	FH	65.9	18.2	27.7	71.3	16.2	87.7
(%)	IC	35.7	23.5	65.8	32.2	<1.0	78.4
	CA	7.9	9.1	113.5	4.8	<1.0	43.3
	L2	6.0	6.4	107.9	3.8	<1.0	39.2
	L4	9.5	10.2	107.3	7.0	1.2	69.8

FH = femoral head.
IC = iliac crest.
CA = calcaneus.
L2 = second lumbar spine.
L4 = fourth lumbar spine.

morphometric parameters might improve the prediction of mechanical properties of bones when combined with global morphometry. Another approach was done by analyzing shape preserved skeletons for orientation analysis of skeletonized trabeculae [7]. Their results showed to be a better measure of trabecular orientation than the classical mean intercept length (MIL) technique. Hence, they were able to show that it is important to analyze trabecular bone structures on an element level. The results from these studies corroborate the importance and the need of local morphometric analyses of trabecular bone structures, as presented in this paper. To our knowledge, this is the first study to analyze single trabecular rod and plate elements in their full volumetric extent.

To validate this new method, three computer-generated models were created and then decomposed and analyzed by local morphometry. A rod, a mixed, and a plate model were chosen to represent a typical range of possible structure types. Spatial decomposition followed by local morphometry of these models gave visually (Fig. 3) and numerically (Table 2) good results.

Visually, the models were decomposed in intuitively correct elements (Fig. 3). Consideration of the figures suggests that the algorithm basically should work on any structure type. Few limitations were found at the interfaces of the plates in the plate model where the interconnecting horizontal plates were encompassed by small wings intuitively belonging to the vertical plates. These artifacts arise from the sharp angles as
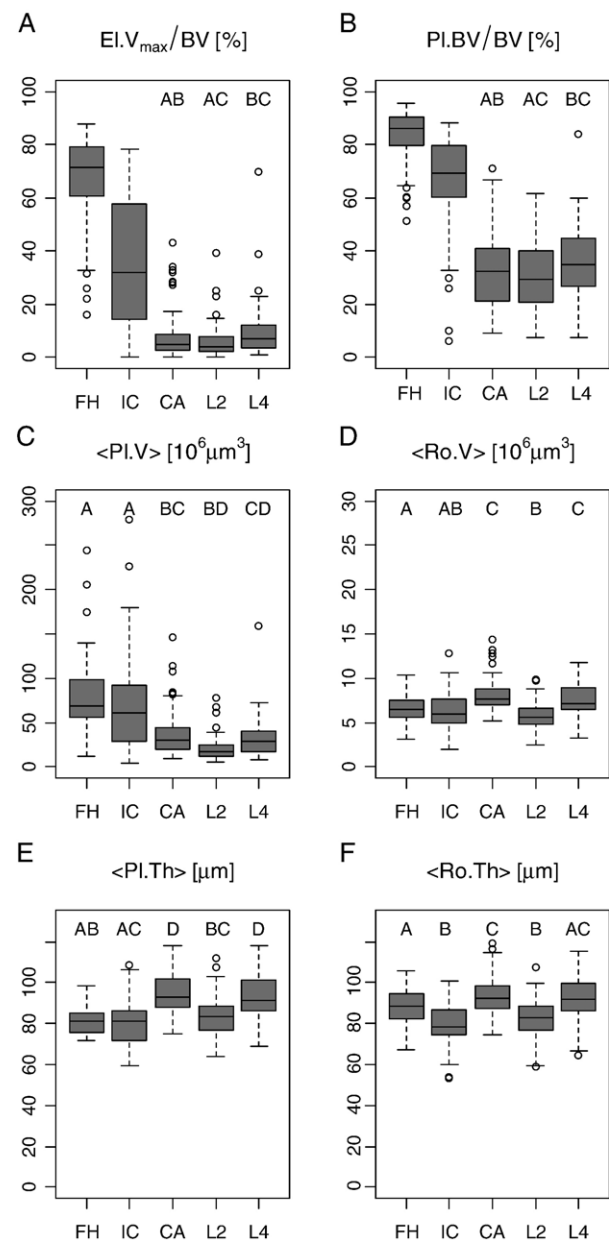

Fig. 5. Box plots of the locally determined indices for the five anatomical sites. (A) Volume of the largest element in percent of the total bone volume, (B) relative amount of plate volume in percentage of the total bone volume. In panels C to F, the distribution of the mean plate (C) and rod (D) volume, and plate (E) and rod (F) thickness as determined by local morphometry is shown.
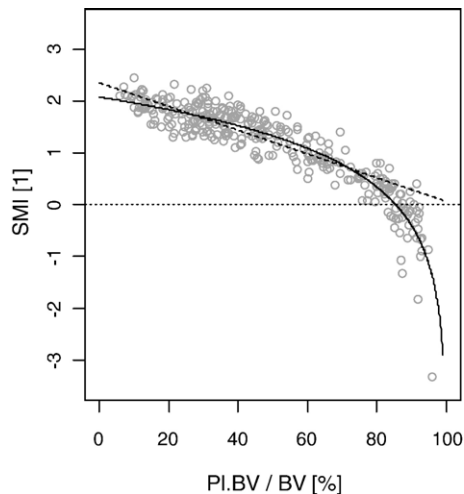
Fig. 6. Relationship of the globally determined structure model index (SMI) with the relative bone volume fraction of plates (Pl.BV/BV). A logarithmic fit (solid line) yields in a high correlation ($R^2 = 0.87$; $P < 0.001$). In the positive SMI range, also a linear fit (dashed line) resulted in a good correlation ($R^2 = 0.81$; $P < 0.001$).

well as from the strict orientation of the plates along the image axes. In realistic structures, we do not expect such ideal configurations and thus, these artifacts should not appear in real data sets. This could also be experimentally validated, where in the analysis of the Biomed I data no such features were detected.

Numerically, the average element volume (<El.V>), surface (<El.S>), and thickness (<El.Th>) as computed by local morphometry were in good agreement to the analytical derived solutions of corresponding models (Table 2). The values for <El.V> and <El.S> all were relatively well centered within the analytic range. However, the already mentioned problem of the shape edges in the plate model was also reflected in the surface values of subscript the plates, where the surface of the interconnecting plates P_C was slightly subscript underestimated (−17%) on the expense of the vertical plates P_A (Fig. 3). The <El. Th> values were all located close to the analytic ranges, where the values for rods were on the lower, and the values for plates on the upper end of the range. These artificial effects are due to the digital nature of the images and are most pronounced in geometrically perfect objects. However, in true bone, there are no perfect rods or plates and it can be assumed that these effects average out such that errors are about the same for all kind of elements.

To demonstrate that this new method does not only work on computer-generated models but also on real human trabecular bone samples, the algorithm was applied to a set of 328 human vertebral bone samples harvested from 70 donors at five different sites (femoral head: FH, iliac crest: IC, calcaneus: CA, second and fourth lumbar spine: L2 and L4). These data have previously been described as part of the European Union BIOMED I Concerted Action "Assessment of Bone Quality in Osteoporosis" [10,34]. All samples could successfully be decomposed into its underlying volumetric rods and plates. Visual inspection showed reasonable results for all structures and sites. As an example, structures from five anatomical sites

of a 37-year-old male donor are visualized in Fig. 4. These images show rod-like structures for calcaneus and the spine samples and a very dense plate-like structure in the femoral head. The sample from iliac crest could either be classified as intermediate or plate-like structure. Where in calcaneus and spine many small elements build up the structure in the femoral head, one big blue element is spanning through the whole sample. Thus, already visual inspection reveals some site differences.

For numerical investigation, the spatially decomposed structures were analyzed by local morphometry. Local morphometry in this sense means that standard global morphometry algorithms were applied to each single element and that these results were averaged for the whole structure independently for all rods and plates, respectively.

We hypothesize that the strength of strong, dense plate-like structures is determined by major elements whereas in spare, loosely connected rod-like structures, the strength is given by the arrangement, quality, and shape of a whole set of elements. Although we did not test bone strength in this project, identification of the largest element within each structure (Fig. 5A) gives evidence for this hypothesis. In FH structures, the strongest elements were in most cases at least half of the total bone volume. Thus, we think it is fair to suggest that these major elements carry most part of the load. In CA, L2, and L4 structures, we found major elements on the order of 5% of the total bone volume (Fig. 5A). Such small elements may only be able to contribute locally to the competence of the specimen. In this case, the arrangement, properties, and quality of the trabecular elements are much more important in determining bone strength. This statement is also supported by the fact that CA, L2, and L4 structures are mostly composed of rod-like elements (Fig. 5B). In mechanical terms, plate-like structures are well suited to bear loads from one defined direction whereas rod-like structures show more flexibility as to the direction of the load. It is generally assumed that the choice which of the two structure types or hybrids thereof is available at a particular site is influenced by the 'local' principal strain axis.

The plates from plate-like structures are generally larger than plates from rod-like structures (Table 3, Fig. 5C) whereas the rods are of about the same size in all structures (Table 3, Fig. 5D). First can be concluded by comparing Fig. 5C, where the mean plate-size in FH and IC structures was significantly higher than in CA, L2, and L4 structures, with Fig. 5B. Thus, plate-like structures do not only have more plate volume but the plates are also larger. This could indicate that in a transformation from a plate-like structure to a rod-like structure plates are reduced in volume, perforated, and finally may become a rod, as was suggested earlier [39]. On the other side, the ranges of the average rod-volume from CA, L2, and L4 structures enclose the ranges of the FH and IC structures (Table 3, Fig. 5D). We therefore think that rods are of about the same size in all structures. We also found that the locally determined mean surface <El.S> of the elements is proportional to the locally determined mean volume <El.V> (Table 3). This is not unexpected, since larger elements also have a larger surface.

The data suggest that the thickness of trabecular elements is to some extent independent of structure and element type and therefore could be a biological constant. This hypothesis is supported by the results of the average thickness measurements for plates (<Pl.Th>) and rods (<Ro.Th>) as shown in Figs. 5E and F. The range of thickness distribution is relatively narrow and the mean values are about the same for rods and plates (Table 3). This finding suggests that the thickness of trabeculae might be an invariant that is determined by biological regulation such as bone remodeling. Evidence for this hypothesis was provided in a study where human parathyroid hormone (PTH) was administered to cynomolgus monkeys [16]. These researchers found that PTH treatment increased cancellous bone volume, which was expressed on an architectural level by increased Tb.N and decreased Tb.Sp with no significant change in Tb.Th. They suggested that thickening of trabeculae may be an early event in response to PTH occurring prior to tunneling, which returns Tb.Th to normal levels while increasing Tb.N. However, this hypothesis could not be proven in our study and needs further biological investigations.

The definition of the structure type of a trabecular bone sample can be improved with local morphometry. This is due to the fact that in local morphometry it is possible to decompose trabecular bone samples in rods and plates and hence, it is possible to compute the relative bone volume fraction of rods (Ro.BV/BV) and plates (Pl.BV/BV = 100% − Ro.BV/BV). We propose to use this measure as a new parameter determining the structure type, where structures with less than 50% Pl.BV/BV will be called rod-like structures and structures with more than 50% Pl.BV/BV will be called plate-like structures. Conventionally, the structure model index (SMI) is used for an estimate of the rod-likeness and plate-likeness of a structure. This parameter was designed to yield values in the range from 0 for perfect plates to 3 for perfect rods [12]. SMI was used in many studies [2,4,6,14,15,17,40] to characterize trabecular bone architecture. In this study, we showed that the globally determined SMI and the locally determined Pl.BV/BV were in good agreement when fitting a logarithmic law ($R^2 = 0.87$, Fig. 6). For positive SMI values, this logarithmic curve was almost linear resulting in a good linear fit for this range ($R^2 = 0.81$, Fig. 6). However, for very dense, plate-like structures, SMI values become negative and thus exceed the definition range. Nevertheless, also these values are true measures and therefore need to be included in the analysis. This is due to the fact that SMI is only a derived parameter depending on the mean surface curvature <H>, the bone volume BV, and the bone surface BS. The relation was shown to equal: SMI = 12<H>BV/BS [17]. Negative SMI values therefore reflect a negative mean curvature or so-called "Swiss cheese" type structures. Opposed to this, Pl.BV/BV cannot exceed its range which is defined from 0% (no rods) to 100% (no plates) and gives therefore an unambiguous classification of structure type. Furthermore, Pl.BV/BV implicitly includes true structural information and provides a measure for the relative amount of rods and plates in a trabecular structure. Opposed to this, a structure with SMI = 1.5 may have a relative amount of plate volume that varies from 20% up to 70% (Fig. 6).

In conclusion, we have developed a new method that allows for the first time a three-dimensional spatial decomposition of porous structures such as trabecular bone in its basic volumetric elements, i.e. plates and rods. The algorithm was validated on computer-generated models where visual and numerical results were in good agreement with corresponding analytical models. Furthermore, 328 human trabecular bone samples from five different anatomical sites could spatially be decomposed and analyzed by local morphometry. We found that in plate-like structures major-elements span through the whole sample giving bone the main mechanical support, whereas in rod-like structures, the mechanical support was determined by the quality, configuration, and shape of a whole set of elements.

Acknowledgments

References

[1] Bernard TM, Manzanera A. Improved low complexity fully parallel thinning algorithm. 10th International Conference on Image Analysis and Processing (ICIAP '99). Venice, Italy; 1999.

[2] Borah B, Dufresne TE, Chmielewski PA, Johnson TD, Chines A, Manhart MD. Risedronate preserves bone architecture in postmenopausal women with osteoporosis as measured by three-dimensional microcomputed tomography. Bone 2004;34:736–46.

[3] Osteoporosis Prevention, Diagnosis, and Therapy. NIH Consensus Statement 2000 March 27–29; 17(1):1–45.

[4] David V, Laroche N, Boudignon B, Lafage-Proust MH, Alexandre C, Ruegsegger P, et al. Noninvasive in vivo monitoring of bone architecture alterations in hindlimb-unloaded female rats using novel three-dimensional microcomputed tomography. J Bone Miner Res 2003;18: 1622–31.

[5] Dequeker J. Assessment of quality of bone in osteoporosis—BIOMED I: fundamental study of relevant bone. Clin Rheumatol 1994;13(Suppl 1): 7–12.

[6] Ding M, Hvid I. Quantification of age-related changes in the structure model type and trabecular thickness of human tibial cancellous bone. Bone 2000;26:291–5.

[7] Gomberg BR, Saha PK, Wehrli FW. Topology-based orientation analysis of trabecular bone networks. Med Phys 2003;30:158–68.

[8] Hafford KJ, Preston KJ. Three-dimensional skeletonization of elongated solids. Comput Vis Graph Image Process 1984;27:78–91.

[9] Hahn M, Vogel M, Pompesius-Kempa M, Delling G. Trabecular bone pattern factor—A new parameter for simple quantification of bone microarchitecture. Bone 1992;13:327–30.

[10] Hildebrand T, Laib A, Müller R, Dequeker J, Rüegsegger P. Direct three-dimensional morphometric analysis of human cancellous bone: microstructural data from spine, femur, iliac crest, and calcaneus. J Bone Miner Res 1999;14:1167–74.

[11] Hildebrand T, Rüegsegger P. A new method for the model-independent assessment of thickness in three-dimensional images. J Microsc 1997; 185:67–75.

[12] Hildebrand T, Rüegsegger P. Quantification of bone microarchitecture with the structure model index. Comput Methods Biomech Biomed Eng 1997;1:15–23.

[13] Hollister SJ, Brennan JM, Kikuchi N. A homogenization sampling procedure for calculating trabecular bone effective stiffness and tissue level stress. J Biomech 1994;27:433–44.

[14] Ito M, Nishida A, Koga A, Ikeda S, Shiraishi A, Uetani M, et al. Contribution of trabecular and cortical components to the mechanical properties of bone and their regulating parameters. Bone 2002;31:351–8.

[15] Ito M, Nishida A, Nakamura T, Uetani M, Hayashi K. Differences of three-dimensional trabecular microstructure in osteopenic rat models caused by ovariectomy and neurectomy. Bone 2002;30:594–8.

[16] Jerome CP, Burr DB, Van Bibber T, Hock JM, Brommage R. Treatment with human parathyroid hormone (1–34) for 18 months increases cancellous bone volume and improves trabecular architecture in ovariectomized cynomolgus monkeys (*Macaca fascicularis*). Bone 2001; 28:150–9.

[17] Jinnai H, Watashiba H, Kajihara T, Nishikawa Y, Takahashi M, Ito M. Surface curvatures of trabecular bone microarchitecture. Bone 2002;30:191–4.

[18] Judex S, Boyd S, Qin YX, Miller LR, Müller R, Rubin C. Combining high-resolution micro-computed tomography with material composition to define the quality of bone tissue. Curr Osteoporos Rep 2003;1:11–9.

[19] Kong TY, Roscoe AW, Rosenfeld A. Concepts of digital-topology. Topol Its Appl 1992;46:219–62.

[20] Kong TY, Rosenfeld A. SURVEY digital topology: introduction and survey. Comput Vis Graph Image Process 1989;48:357–93.

[21] Lee T, Kashyap L. Building skeleton models via 3-D medial surface/axis thinning algorithms. CVGIP, Graph Models Image Process 1994;56:462–78.

[22] Lobregt S, Verbeek PW, Groen FCA. Three-dimensional skeletonization: principle and algorithm. IEEE Trans Pattern Anal Mach Intell PAMI-2 1980:75–7.

[23] Ma CM. On topology preservation in 3D thinning. CVGIP, Image Underst 1993;59:328–39.

[24] Majumdar S. Magnetic resonance imaging of trabecular bone structure. Top Magn Reson Imaging 2002;13:323–34.

[25] Majumdar S. A review of magnetic resonance (MR) imaging of trabecular bone micro-architecture: contribution to the prediction of biomechanical properties and fracture prevalence. Technol Health Care 1998;6:321–7.

[26] Manzanera A, Bernard TM, Prêteux F, Longuet B. Medial faces from a concise 3D thinning algorithm. Proceedings of the Seventh IEEE International Conference on Computer Vision (ICCV '99). Kerkyra, Greece: IEEE Computer Society; 1999. p. 337–43 [Sept. 20–27].

[27] Manzanera A, Bernard TM, Prêteux F, Longuet B. Ultra-fast skeleton based on an isotropic fully parallel algorithm. Proceedings of the 8th International Conference on Discrete Geometry for Computer Imagery '99. Lecture Notes in Computer Science, vol. 1568. London, UK: Springer-Verlag; 1999. p. 313–24.

[28] Manzanera A, Bernard TM, Prêteux F, Longuet B. A unified mathematical framework for a compact and fully parallel n-D skeletonization procedure. Proceedings SPIE Conference 3811 on Vision Geometry VIII. Denver, CO; 1999.

[29] Morgenthaler DG. Three-dimensional digital topology: the genus, TR-980. College Park: University of Maryland; 1980.

[30] Morgenthaler DG. Three-dimensional simple points: serial erosion. Parallel thinning, and skeletonization, TR-1005. College Park: University of Maryland; 1981.

[31] Mosekilde L. Age-related changes in vertebral trabecular bone architecture —Assessed by a new method. Bone 1988;9:247–50.

[32] Müller R. The Zürich experience: one decade of three-dimensional high-resolution computed tomography. Top Magn Reson Imaging 2002;13:307–22.

[33] Müller R, Hildebrand T, Rüegsegger P. Non-invasive bone biopsy: a new method to analyse and display the three-dimensional structure of trabecular bone. Phys Med Biol 1994;39:145–64.

[34] Müller R, Rüegsegger P. Micro-tomographic imaging for the nondestructive evaluation of trabecular bone architecture. Stud Health Technol Inform 1997;40:61–79.

[35] Müller R, van Lenthe G. Microarchitectural aspects of quality and competence of bone. Adv Osteoporotic Fract Manag 2004;3:2–12.

[36] Odgaard A. Three-dimensional methods for quantification of cancellous bone architecture. Bone 1997;20:315–28.

[37] Parfitt AM. Trabecular bone architecture in the pathogenesis and prevention of fracture. Am J Med 1987;82:68–72.

[38] Parfitt AM, Drezner MK, Glorieux FH, Kanis JA, Malluche H, Meunier PJ, et al. Bone histomorphometry: standardization of nomenclature, symbols, and units. Report of the ASBMR Histomorphometry Nomenclature Committee. J Bone Miner Res 1987;2:595–610.

[39] Parfitt AM, Mathews CH, Villanueva AR, Kleerekoper M, Frame B, Rao DS. Relationships between surface, volume, and thickness of iliac trabecular bone in aging and in osteoporosis. Implications for the microanatomic and cellular mechanisms of bone loss. J Clin Invest 1983;72:1396–409.

[40] Patel V, Issever AS, Burghardt A, Laib A, Ries M, Majumdar S. MicroCT evaluation of normal and osteoarthritic bone structure in human knee specimens. J Orthop Res 2003;21:6–13.

[41] Pothuaud L, Laib A, Levitz P, Benhamou CL, Majumdar S. Three-dimensional-line skeleton graph analysis of high-resolution magnetic resonance images: a validation study from 34-microm-resolution micro-computed tomography. J Bone Miner Res 2002;17:1883–95.

[42] Pothuaud L, Porion P, Lespessailles E, Benhamou CL, Levitz P. A new method for three-dimensional skeleton graph analysis of porous media: application to trabecular bone microarchitecture. J Microsc 2000;199:149–61.

[43] Pothuaud L, Van Rietbergen B, Mosekilde L, Beuf O, Levitz P, Benhamou CL, et al. Combination of topological parameters and bone volume fraction better predicts the mechanical properties of trabecular bone. J Biomech 2002;3:1091–9.

[44] Rosenfeld A. Three-dimensional digital topology, TR-936. College Park: University of Maryland; 1980.

[45] Rüegsegger P, Koller B, Müller R. A microtomographic system for the nondestructive evaluation of bone architecture. Calcif Tissue Int 1996;58:24–9.

[46] Saha PK, Chaudhuri BB. 3 D digital topology under binary transformation with applications. Comput Vis Image Underst 1996;63:418–29.

[47] Saha PK, Chaudhuri BB. Detection of 3-D simple points for topology preserving transformations with application to thinning. IEEE Trans Pattern Anal Mach Intell 1994;16:1028–32.

[48] Saha PK, Chaudhuri BB, Majumder DD. A new shape preserving parallel thinning algorithm for 3 D digital images. Pattern Recogn 1997;30:1939–55.

[49] Saha PK, Gomberg BR, Wehrli FW. Three-dimensional digital topological characterization of cancellous bone architecture. Int J Imaging Syst Technol 2000;11:81–90.

[50] van Rietbergen B, Weinans H, Huiskes R, Odgaard A. A new method to determine trabecular bone elastic properties and loading using micromechanical finite-element models. J Biomech 1995;28:69–81.

[51] Wehrli FW, Saha PK, Gomberg BR, Song HK, Snyder PJ, Benito M, et al. Role of magnetic resonance for assessing structure and function of trabecular bone. Top Magn Reson Imaging 2002;13:335–55.

[52] Wu QJ, Bourland JD. Three-dimensional skeletonization for computer-assisted treatment planning in radiosurgery. Comput Med Imaging Graph 2000;24:243–51.

[53] Zysset PK. A review of morphology-elasticity relationships in human trabecular bone: theories and experiments. J Biomech 2003;36:1469–85.